Volume 13
Number 38
14 October 2025
Pages 31805–32922

# Journal of Materials Chemistry A

Materials for energy and sustainability

rsc.li/materials-a

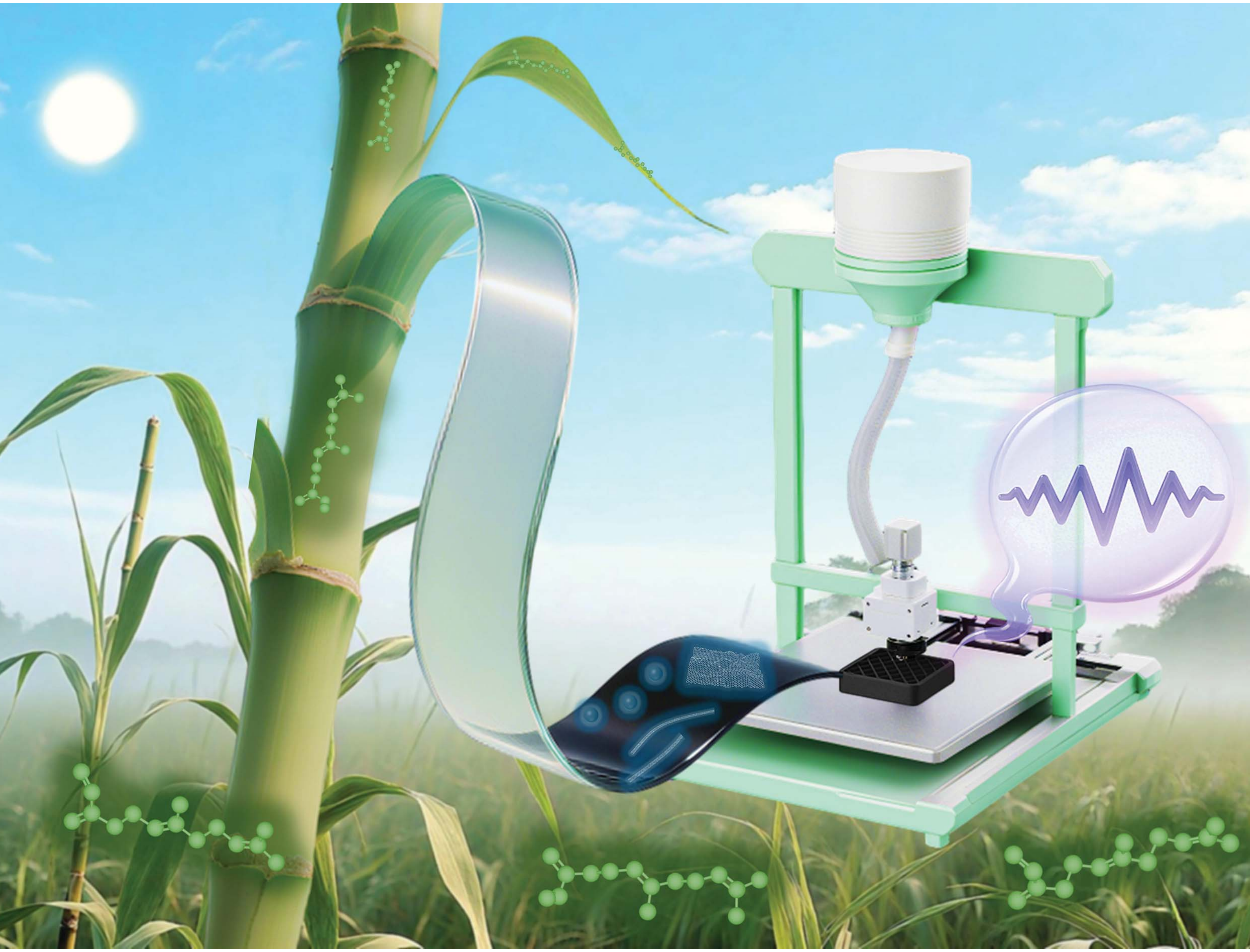

ISSN 2050-7488

ROYAL SOCIETY OF CHEMISTRY

**PAPER**
Weinan Xu *et al.*
Sustainable thermoplastic elastomer-based nanocomposites and their 3D printing for flexible and stretchable sensors

Journal of
Materials Chemistry A

PAPER

View Article Online
View Journal | View Issue

Cite this: *J. Mater. Chem. A*, 2025, **13**, 32134

# Sustainable thermoplastic elastomer-based nanocomposites and their 3D printing for flexible and stretchable sensors

Xun Liu, Naifu Shen, Jinyu Bu, Muxuan Yang, Xin Guan and Weinan Xu †*

Stretchable and wearable electronics and devices have brought unprecedented opportunities for many applications including robotics, biomedicine, and artificial intelligence. The fundamental materials that enable such applications generally involve soft conductors that combine conductive nanofillers with soft matrices. However, most current soft conductors rely on conventional soft elastomers such as silicone rubber and polyurethane, which are produced from petrochemicals with limited sustainability. In this study, we developed a series of soft nanocomposites based on the integration of sustainable biobased thermoplastic elastomer polystyrene-*b*-polyfarnesene-*b*-polystyrene (SFS) with carbon nanofillers of different dimensions (2D graphene, 1D carbon nanotubes, or 0D carbon black). Importantly, SFS and its nanocomposites are fully compatible with extrusion-based 3D printing. We demonstrated pellet 3D-printing of SFS nanocomposites into functional and customizable 3D structures. The mechanical and electrical properties and dynamic responses to mechanical deformation of SFS nanocomposites were systematically investigated for their promising applications in wearable sensors and environment monitoring. We found that the type/geometry of carbon nanofillers, the ratio between different types of nanofillers, and processing conditions (3D printing *vs.* casting) have significant effects on the electrical properties and strain sensor performance. Such 3D printable soft and sustainable nanocomposites provide a new material platform for applications in soft electronics/robotics and human–machine interfaces.

Received 9th June 2025
Accepted 24th July 2025

DOI: 10.1039/d5ta04676a

rsc.li/materials-a

## 1. Introduction

Stretchable and wearable electronics and sensors are critical components in human–machine interfaces and soft robotics.[1–4] In order to fabricate such soft and stretchable electronics and sensors, one critical component is materials that are stretchable and conductive and have fast and tunable responses to mechanical deformation.[5,6] The most common method to achieve such properties is by combining a soft elastomer matrix with electrically conductive nanofillers. The commonly used

---

*School of Polymer Science and Polymer Engineering, The University of Akron, Akron, OH 44325, USA. E-mail: wxu18@utk.edu*

† Present address: Department of Materials Science and Engineering, The University of Tennessee, Knoxville, TN 37996, USA.

**Weinan Xu**

*Dr Weinan Xu is currently an assistant professor in the Department of Materials Science and Engineering at the University of Tennessee, Knoxville. He obtained his PhD degree in Materials Science and Engineering from the Georgia Institute of Technology and did his postdoctoral research at Johns Hopkins University. He then started his independent career at the School of Polymer Science and Polymer Engineering at the University of Akron before moving to Tennessee. His current research focuses on the development of sustainable/functional polymer composites and their advanced manufacturing, with applications in energy, electronics, and biomedicine. He has been recognized with several awards, including the DARPA Young Faculty Award, Polymer Processing Society Early Career Award, NSF LEAP award, and Best PhD Thesis Award from Sigma Xi and Georgia Tech.*

soft matrices for such purposes include silicone elastomers (polydimethylsiloxane),[7,8] polyurethane,[9] natural rubber,[10–12] synthetic rubber,[13] thermoplastic elastomers (TPEs)[14] and certain types of hydrogels.[15,16] The commonly used conductive nanofillers include metal nanoparticles (NPs),[17,18] nanowires,[19] carbon nanomaterials,[20–23] and liquid metals.[24]

Despite the significant progress and excellent performance achieved for such conventional conductive soft nanocomposites, there are several key issues that need to be addressed. Firstly, most of the current elastomers used as soft matrices are chemically synthesized from petrochemicals, whose sustainability and recyclability are usually very limited.[25] Secondly, the majority of the elastomers and their nanocomposites are not compatible with 3D printing technologies due to their chemically crosslinked structure or unsuitable rheological properties. Thirdly, it is challenging to achieve high sensitivity and stability for both small strains and large strains in the same soft nanocomposite system.[26]

To overcome these limitations, in this study, we develop a new soft and 3D printable nanocomposite system based on biobased sustainable TPEs and their composites with the incorporation of multiple types of carbon nanomaterials. TPEs are a category of polymers that combines rubber elasticity with melt processability of thermoplastics.[27,28] This is enabled by their unique molecular structures which contain both a soft elastic/rubbery block and a hard block; the hard blocks act as physical crosslinks to enhance their mechanical strength and stability. One of the most commonly used types of TPEs is styrenic TPEs which have a rubbery soft block and polystyrene hard block; representative examples include polystyrene-*b*-polyethylene/butylene-*b*-polystyrene (SEBS), polystyrene-*b*-polybutadiene-polystyrene (SBS), and poly(styrene-*b*-isobutylene-*b*-styrene) (SIBS).[29] However, these conventional styrenic TPEs are based on chemical synthesis with petrochemicals, which have limitations in terms of sustainability and life cycle.

In recent years, biomass-derived materials and monomers have been used for the synthesis of TPEs,[30,31] which provides a new method to enhance the sustainability and carbon emission of TPE production.[32,33] Terpenes, which are naturally abundant and originate from plants are well-suited to this purpose. For instance, one important type of terpene, β-farnesene, which can be derived from the fermentation of sugar from natural plants, especially sugar cane,[34,35] has been utilized as a biobased monomer to copolymerize with styrene to synthesize new types of styrenic TPEs.[36,37] Such farnesene-based sustainable TPEs will be used as the soft and functional matrix in our study.

Besides their benefits in material sustainability, the use of functional TPEs as the soft matrix for soft electronics/sensors also makes it possible to use 3D printing as a novel method for their fabrication.[38,39] Compared with conventional processing and fabrication such as casting, molding, or extrusion, 3D printing of polymer composites enables customizable and complex 3D geometry fabrication[40–42] and results in less material waste,[43,44] low tooling cost and reduced lead time.[45–47] The use of 3D printing technologies for the fabrication of soft and wearable sensors is becoming more and more popular, as demonstrated by many recent reports.[48,49] Due to the melt processability of TPEs and their composites, theoretically, they are compatible with extrusion-based 3D printing. However, the most commonly used extrusion-based method, *i.e.* fused filament fabrication (FFF), is generally not suitable for printing soft elastomers and composites due to issues such as filament buckling, poor object/bed adhesion, and unsuitable melt viscosity.[50,51] Direct ink writing (DIW) has also been used to fabricate 3D composite structures with TPEs as the soft matrix and showed unique dielectric and optical properties.[52,53] But the DIW method requires the use of organic solvents and rheological modifiers, which are not desirable for many applications.[54,55]

Pellet extrusion-3D printing can potentially overcome these issues and be used for the fabrication of soft electronics/sensors. Compared with the conventional FFF method, the pellet-extrusion method can directly use polymer pellets as the feedstock, which are loaded into an extruder that is directly connected to the printing head.[56] Pellet 3D printing also reduces thermal degradation compared to FFF, which helps maintain its structure and physical properties.[57,58] Moreover, it has major advantages of scalability and time and cost savings. It does not require the filament fabrication step, which significantly reduces production time and raw materials cost. Although pellet 3D printing exhibits these major advantages, its adoption in the fabrication of soft/stretchable devices using elastomer composites has not been investigated in detail, and this direction holds great potential for further expanding the applications of pellet 3D printing.

In this work, we developed a new sustainable and 3D-printable nanocomposite system that has excellent elasticity, stretchability, tunable internal structures, and strain-dependent electrical properties. Our soft nanocomposites are based on the integration of polystyrene-*b*-polyfarnesene-*b*-polystyrene (SFS) with two types of carbon nanofillers (carbon nanotubes and graphene or carbon nanotubes and carbon black) with different geometries. Importantly, these soft nanocomposites are fully compatible with pellet 3D printing, which enables the fabrication of customizable and functional structures. The SFS nanocomposites show excellent stretchability (>1500%), a comparable modulus to human skins,[59] and highly tunable electrical conductivity. Their electrical responses to mechanical strain are highly dependent on the nanofiller types and ratio, nanofiller loading, and composite processing techniques. Very high gauge factors (GFs) of over 3000 can be achieved for strains in the range of 300–500%. We also demonstrate that these SFS nanocomposites can be used for human motion sensing and environment monitoring with high and consistent performance.

## 2. Experimental section

### 2.1 Materials

The SFS polymer (SEPTON BIO SF904) was provided by Kuraray Co. and carbon black (BP2000) was purchased from Cabot. Multiwalled carbon nanotubes were purchased from MSE Supplies (outer diameter: 10–15 nm, purity >99%) and graphene was purchased from Tianyuan Empire (no. of layers: 1–4 (≥95%)). Toluene and other solvents were purchased from Fisher Scientific. All chemicals were used as received without further purification.

### 2.2 SFS nanocomposite and pellet preparation

The carbon nanomaterials (CNTs and CB, or CNTs and graphene) were mixed in a predetermined ratio and then dispersed in toluene. The solution was bath sonicated for 1 hour to achieve homogeneous dispersion of the nanofillers. Then a corresponding amount of the SFS polymer was added to the solution and stirred until the polymer was completely dissolved. The composite solution was then cast into a glass Petri dish and the solvent was evaporated to form a solid composite membrane. The composite membrane was then cut into small pieces ($4 \times 4$ mm) with scissors and used as the feeding stock for pellet 3D printing.

### 2.3 Pellet extrusion 3D printing

SFS or its composite pellets were loaded into the hopper of a desktop pellet-extrusion 3D printer (Tumaker NX Pro). The printer is equipped with two vertically aligned miniature screw extruders for extruding granules. Two independent heating zones in each extruder provide accurate temperature control. The screw has a diameter of 8 mm, an $L/D$ ratio of 7.5, and a compression ratio of 1.7 : 1. The printing nozzle diameter is 800 μm. The printing temperature was set at 175 °C for pristine SFS and 205 °C for SFS nanocomposites. The build plate temperature was set at 80 °C. The layer height was set at 0.2 mm. The printing speed can be varied from 4 to 20 mm $s^{-1}$. The printing head moves in the $x$ and $y$ directions controlled by a digital model while the build plate moves in the $z$ direction. The 3D models were built using SolidWorks and the slicing was done with SuperSlicer.

### 2.4 Characterization

Scanning electron microscopy (SEM) was conducted using a JEOL-7401 FE-SEM at 5 kV accelerating voltage. Fourier transform infrared (FTIR) spectra were collected (Nicolet iS50, Thermo Scientific) in attenuated total reflection mode. The data were an accumulation of 128 scans at a resolution of 4 $cm^{-1}$ in the range of 4000–400 $cm^{-1}$. GPC experiments were carried out using a Tosoh EcoSEC HLC-8320 with THF as the solvent at a flow rate of 1 mL $min^{-1}$ and 40 °C. Thermal stability was studied by thermogravimetric analysis (TGA) (TA Q50). The temperature range was from room temperature to 600 °C at a heating rate of 10 °C $min^{-1}$. The experiment was conducted under a nitrogen atmosphere. Hardness was determined with a Shore A digital hardness tester according to ISO 868-1986. Raman spectra were collected with a Renishaw inVia confocal Raman microscope with an excitation wavelength of 514 nm. Differential scanning calorimetry (DSC) was performed on a TA Instruments Q200 with aluminum hermetic pans. Tensile tests were conducted with an Instron 5567 tensile tester according to the ISO 37 standard procedure. The electrical properties of the nanocomposites and strain sensor performance were measured using a Keithley 2400 source meter. Programmed or cyclic stretching and relaxing were done with a custom-built automated biaxial stage with AC brushless servo motors (Parker Hannifin SM231AL-NPSN).

## 3. Results and discussion

### 3.1 Structure and properties of sustainable SFS elastomers

The TPE used in our study is a triblock copolymer composed of biobased monomer β-farnesene and styrene. Its synthesis and chemical structure are shown in Fig. 1a. The two blocks at both ends are polystyrene, and the middle block is polyfarnesene, so it is named SFS in this manuscript (S stands for polystyrene and F stands for polyfarnesene). The hard polystyrene blocks act as physical crosslinks to enhance the mechanical strength and stability of SFS. The molar mass of SFS ($M_n = 54.0$ kDa, $Đ = 1.24$, see Fig. S1) was determined using GPC. The weight fraction of the polystyrene block of SFS in our study is 21%, and the elastomer has a hardness of 25 Shore A. The main role of the polystyrene (PS) block is to enhance the mechanical strength, while maintaining the melt processability of the resulting copolymer. The middle polyfarnesene block is hydrogenated to enhance the thermal and chemical stability of the SFS copolymers. From the chemical structure of SFS, it can be seen that the β-farnesene repeating unit forms short branches from the backbone; this unique bottlebrush-like structure in the soft middle block further contributes to the softness and flexibility of SFS.

We systematically characterized the structure and properties of SFS. The $^1$H NMR spectrum confirms the chemical structures of SFS with the corresponding locations labeled (Fig. 1b). The DSC data (Fig. 1c) show two glass transition temperatures; the one at −66 °C corresponds to the glass transition of the polyfarnesene block and the one at 100 °C corresponds to the glass transition of the polystyrene block. The broad exothermic peak at about 35 °C is attributed to the twisting and alignment of the aromatic centers along an ordered axis of the polystyrene block.[60] AFM characterization of SFS (Fig. 1c inset) shows well-defined microphase-separated morphology between the polystyrene and polyfarnesene blocks. The bright spherical domains correspond to PS and the dark matrix corresponds to the polyfarnesene domain.

One of the most important features for choosing SFS as the polymer matrix for the fabrication and 3D printing of soft sensors is its mechanical properties. The representative tensile stress–strain curves of SFS (samples prepared by compression molding at 165 °C for 60 min) are shown in Fig. 1d. SFS shows an average tensile strength of 5.0 MPa, elongation at break of 1030%, Young's modulus of 0.9 MPa, and M100 modulus (strength at 100% elongation) of 0.35 MPa. The SFS material exhibits a relatively low modulus, making it highly suitable for use in soft and wearable sensors and devices that require excellent compliance and comfort when in contact with the human body. These mechanical properties are better (especially higher elongation at break) or comparable with those of other commonly used soft materials for flexible sensors and electronics including PDMS and polyurethane.[7,61]

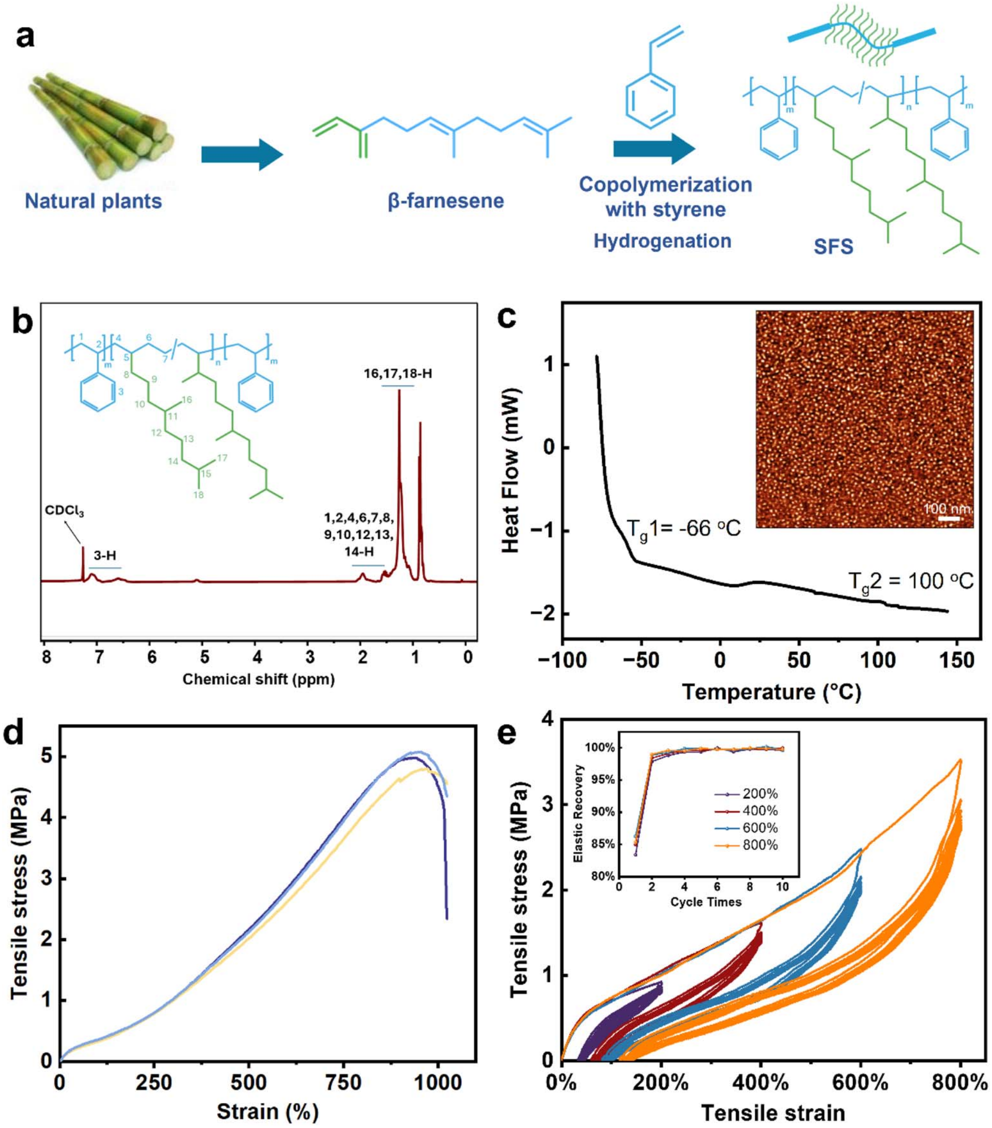

Fig. 1 (a) Schematic of the synthesis and chemical structure of the SFS elastomer. (b) $^1$H NMR spectrum of SFS. (c) DSC of SFS shows two glass transitions of the hard and soft blocks. The inset shows the AFM phase image of a SFS thin film. (d) Representative tensile stress–strain curves of SFS. (e) Cycling tests of SFS with a maximum strain of 200%, 400%, 600%, and 800% at a rate of 200 mm min$^{-1}$; ten cycles of testing at each maximum strain are shown. The inset shows the elastic recovery ratio of SFS during the cyclic tests with different maximum strains.

Cyclic tensile testing with different maximum strains was also conducted on SFS (Fig. 1e); it can be seen that after the first loading–unloading cycle, the 2nd loading shows an obvious softening or decrease in the modulus, and then the following cycles closely match each other. This can be explained by the classic Mullins effect.[61–63] During the first stretching, there is some extent of disentanglement of polymer chains and physical crosslinking, as well as slippage of molecular chains, so that hysteresis under cyclic loading and strain-softening occur.[64] The elastic recovery ratio of SFS during the cyclic tests is shown in the Fig. 1e inset, which further shows that after the first loading cycle, SFS remains stable and fully reversible (>99% recovery) against mechanical deformation, which is beneficial for its application in flexible electronics and sensors.

### 3.2 Pellet 3D printing of the SFS elastomer

The SFS elastomer and its nanocomposites are compatible with extrusion-based 3D printing because they are not chemically crosslinked. The most commonly used method for extrusion-based 3D printing is fused filament fabrication (FFF), which involves the melting and extrusion of a plastic filament from a heated nozzle on the platform in a layer-by-layer manner. However, FFF is not suitable for printing soft elastomers because soft filaments cannot be consistently and continuously extruded without buckling. Moreover, the filament fabrication process adds additional cost and time to the process. In this study, we overcome this issue by using pellet 3D printing for SFS and its composites. In comparison with FFF, pellet 3D printing (Fig. 2a) can use polymer pellets directly without the need for filament fabrication, which reduces production time and raw

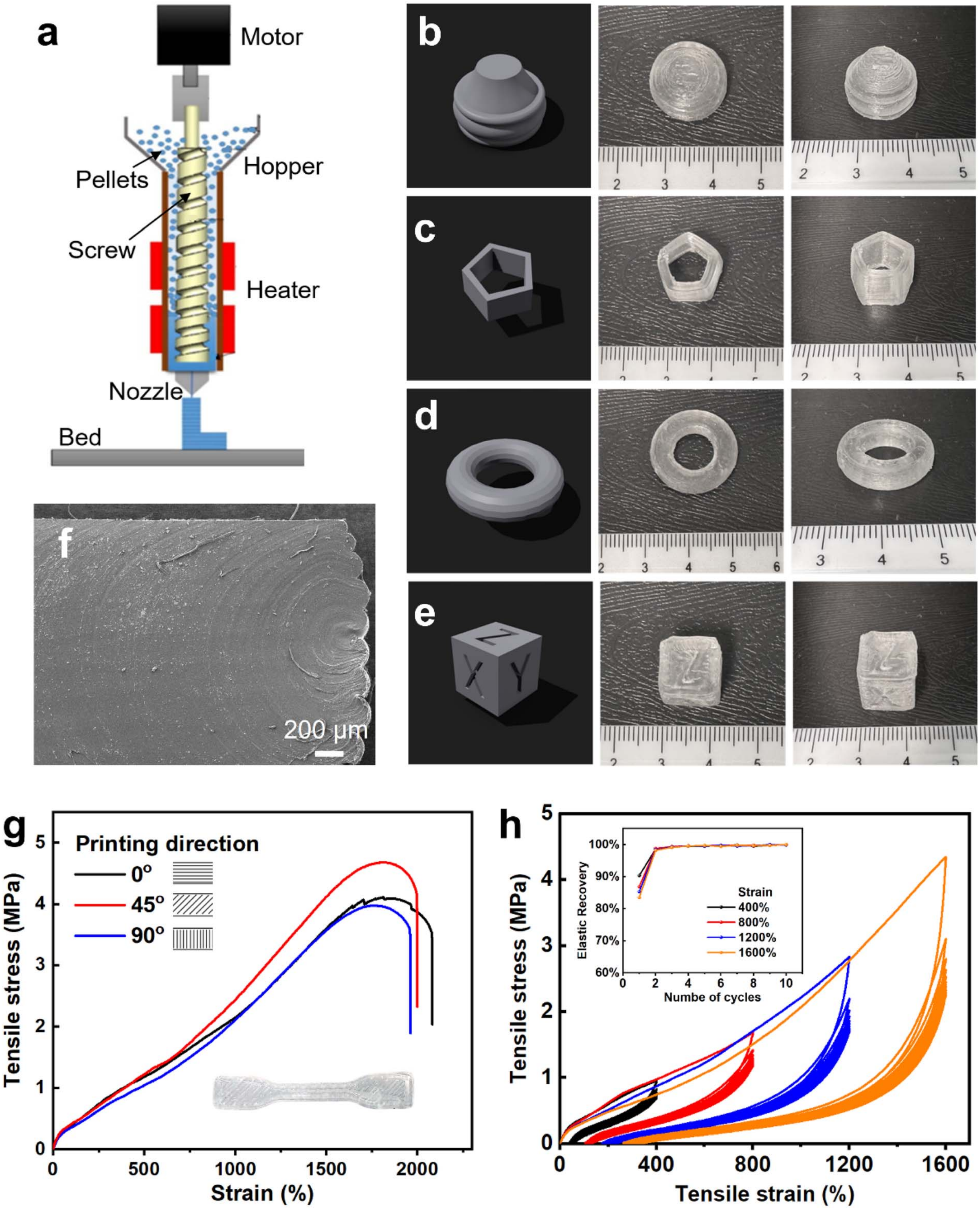

Fig. 2 (a) Schematic of pellet-extrusion 3D printing. (b–e) Representative 3D structures printed from SFS pellets, including (b) inverted bowl, (c) pentagonal prism, (d) circular tube, and (e) cubic dice. The first column is the 3D model, the second column is the top view, and the third column is the tilted view. (f) Cross-section SEM of the 3D-printed SFS structure. (g) Representative stress–strain curves of pellet 3D-printed SFS with different printing directions. The inset shows a photo of a typical 3D-printed dogbone with a 45° printing direction. (h) Cycling tests of 3D-printed SFS with a maximum strain of 400%, 800%, 1200%, and 1600% at a rate of 200 mm min$^{-1}$; ten cycles of testing at each maximum strain are shown. The inset shows the elastic recovery ratio of SFS during the cyclic tests with different maximum strains.

materials cost. Moreover, it enables a broader selection of materials. Soft TPEs such as SFS are fully compatible with the printing process.

The main parameters that need to be controlled and optimized during pellet 3D printing of SFS include loading chamber temperature (inside the single screw extruder), nozzle temperature, and printing bed temperature, which are set at 150 °C, 175 °C, and 80 °C, respectively. The nozzle diameter is 0.8 mm and layer height is set at 0.2 mm. These parameters are determined after varying them in a range and optimization based on the final printing quality. Representative 3D structures with different geometries such as inverted bowl and pentagonal prism are shown in Fig. 2b–e. High printing quality and shape fidelity are achieved, and the difference between actual dimensions and the corresponding digital model is within 3%. The pellet 3D-printed structures also have dense and solid internal structures, as shown in the cross-section SEM image in Fig. 2f. The surface and edge of the printed structure still show layered morphology that is typical for extrusion-based 3D printing (Fig. S2).

We also studied the mechanical properties of SFS structures fabricated by pellet 3D printing (printing temperature of 175 °C). It is known that the mechanical properties of 3D structures by extrusion-based 3D printing generally depend on the printing direction. For instance, for the pellet 3D-printed dogbone samples, a printing direction of 0°, 90°, or 45° means that the traveling path of the printing nozzle is parallel, perpendicular, or has a 45° angle in reference to the long axis of the dogbone. Tensile testing of the samples printed with these three directions shows very similar mechanical properties (Fig. 2g). For instance, the average tensile strength is 4.69, 4.63, and 4.11 MPa for samples with printing directions of 0°, 45°, and 90°, respectively. The average Young's modulus for the samples with a printing direction of 0°, 45°, and 90° is 1.10, 0.89, and 0.89 MPa, respectively. These values are also very close to those of SFS structures made by compression molding.

Interestingly, the elongation at break for the pellet 3D-printed samples is about 2000%, which is much higher than that of compression-molded SFS (about 1000%, Fig. 1d). The main reason for such a difference is probably that during pellet 3D printing, SFS chains are thermally processed in the extruder for a longer time compared with compression molding. This thermal annealing effect leads to a denser and better-ordered internal structure. Cyclic tensile testing with different maximum strains was also conducted on pellet 3D-printed SFS (Fig. 2h, see also Fig. S3). Obvious hysteresis and strain-softening occur during the first stretching, and then the structure becomes stable and fully recoverable during subsequent mechanical deformation with an elastic recovery ratio over 99%.

### 3.3 SFS nanocomposites and their morphologies

In order to make soft and conductive structures and devices with SFS as the matrix, we incorporated carbon nanomaterials as nanofillers into SFS. The commonly used carbon nanomaterials as conductive fillers include graphene, multiwall carbon nanotubes (CNTs), and carbon black (CB), which belong to 2D, 1D, and 0D nanomaterials, respectively. We initially tested with only graphene as the nanofiller, but the conductivity of SFS-graphene composites is relatively low ($10^{-5}$ S m$^{-1}$) even with the incorporation of 10 wt% graphene (Fig. S4). In order to achieve higher electrical conductivity and sensitivity, in this study, we focused on combining two types of carbon nanomaterials (CNTs and graphene, or CNTs and CB) into the SFS matrix to create flexible and conductive nanocomposites. The integration of two types of nanofillers also enables a wider range of electrical properties and strain responses of the nanocomposites, as shown in the next section. Besides enhancing the physical properties, the combination of two types of carbon nanofillers also has the benefits of decreasing the overall cost of such nanocomposites, because CB has a much lower price than graphene or CNTs.[65,66]

The carbon nanomaterials were mixed with SFS by solution blending and then the nanocomposites can be prepared by two different methods: solution casting or pellet 3D printing (Fig. 3a). We focus on two types of nanocomposites with different combinations of carbon nanofillers: SFS/CNT/CB represents SFS composites with CNTs and CB incorporated and SFS/CNT/Gr represents SFS composites with CNTs and graphene incorporated; the weight ratio between these components is indicated by the number in the bracket after the name such as SFS/CNT/CB (90/3/7). TEM images of the three types of carbon nanomaterials (Fig. 3b–d) confirm their morphologies and dimensions. The lateral size of graphene is from hundreds of nm to several μm; the diameter of CNTs is about 10 nm; the average size of CB is about 20–30 nm.

The internal structures of the nanocomposites were studied by cross-section SEM (Fig. 3e and f). The SFS/CNT/CB composite shows a high density of fiber-like CNTs and CB NPs, which have a relatively good dispersion in the SFS matrix, and the CB NPs can form local aggregates. On the other hand, the SFS/CNT/Gr (90/5/5) composite shows quite different morphology with 2D graphene nanoflakes clearly visible. The total weight percentage of the carbon nanofillers in the composites remained at 10 wt%; this is confirmed by the TGA analysis (Fig. 3h), which shows that the residual weight at 500 °C is very close to 10%. The ratio between the two types of nanofillers (CNT : CB or CNT : Gr) was also varied and optimized based on the electrical resistance and sensitivity achieved in the nanocomposites, as will be discussed in the next section. The two types of nanocomposites we will focus on are SFS/CNT/CB (90/3/7) and SFS/CNT/Gr (90/5/5). Raman spectra of these carbon nanomaterials and the SFS nanocomposites show the characteristic peaks of graphene, CNTs and CB. (Fig. S5).

The SFS-based nanocomposites are still highly flexible and stretchable, as shown by the bending, twisting, and stretching demonstrations in Fig. 3g. The mechanical properties of the nanocomposites fabricated by both solution casting and pellet 3D printing (printing temperature of 205 °C) were studied and compared. The representative tensile stress–strain curves for SFS/CNT/CB (90/3/7) nanocomposites are shown in Fig. 3i. Compared with pristine SFS (Fig. 1d), the SFS nanocomposites show a higher modulus and higher elongation at break due to the reinforcement of the carbon nanofillers. For instance, the

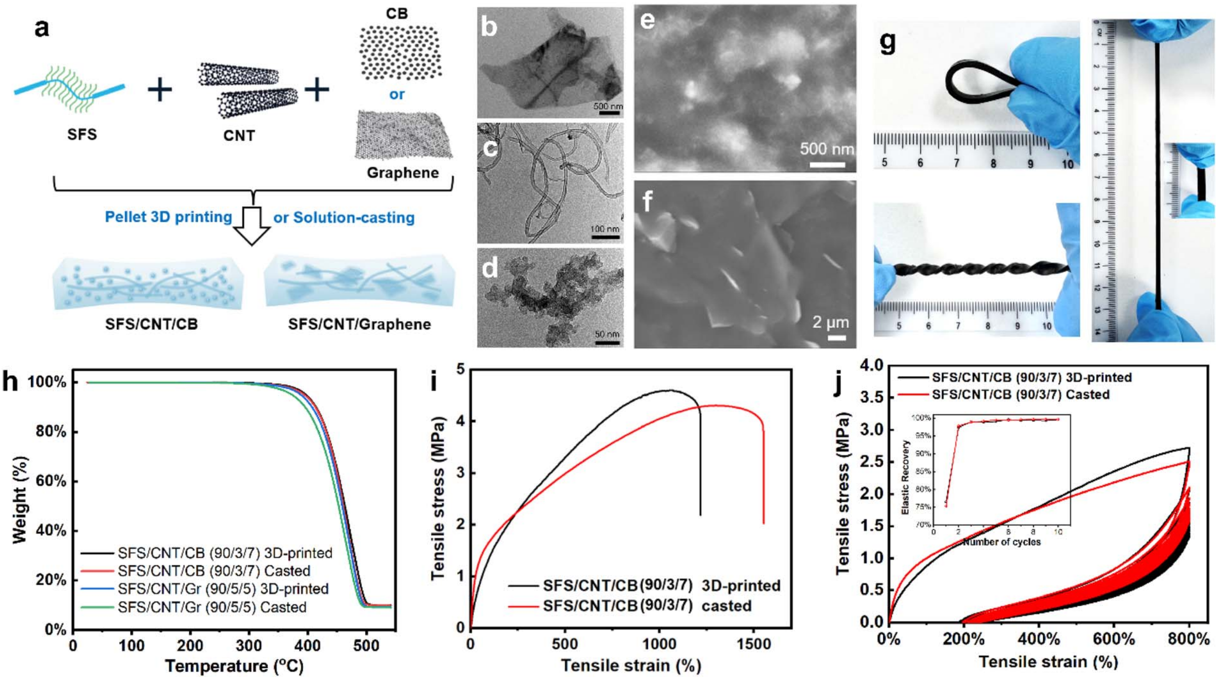

Fig. 3 (a) Schematic of the SFS-based nanocomposite fabrication process. (b–d) TEM images of graphene (b), CNTs (c), and carbon black (d). (e and f) Cross-section SEM images of SFS/CNT/CB (90/3/7) (e) and SFS/CNT/Gr (90/5/5) (f) nanocomposites. (g) Demonstration of the mechanical flexibility and stretchability of the SFS/CNT/CB (90/3/7) nanocomposite. (h) TGA curves for the different types of SFS-based nanocomposites fabricated by pellet 3D printing or solution casting. (i) Representative tensile stress–strain curves for SFS/CNT/CB (90/3/7) fabricated by pellet 3D printing and solution casting. (j) Cycling tests of SFS/CNT/CB (90/3/7) with a maximum strain of 800%; ten testing cycles at the maximum strain are shown. The inset shows the elastic recovery ratio of SFS/CNT/CB (90/3/7) during the cyclic test.

SFS/CNT/CB (90/3/7) nanocomposite fabricated by solution casting shows a Young's modulus of 44.9 MPa, M100 modulus of 1.68 MPa, and elongation at break of 1550%.

Moreover, the fabrication method also has substantial effects on the mechanical properties of SFS nanocomposites. The SFS/CNT/CB (90/3/7) nanocomposite fabricated by solution casting shows similar tensile strength (4.3 MPa *vs.* 4.6 MPa), higher modulus (1.68 MPa *vs.* 1.38 MPa M100 modulus) and higher elongation at break (1550% *vs.* 1220%) compared with the samples prepared by pellet 3D printing. Cyclic tensile testing on SFS/CNT/CB (90/3/7) fabricated by both solution casting and pellet 3D printing was conducted (Fig. 3j). It can be seen that they show almost identical properties, with obvious hysteresis during the first stretching cycle, and then maintain highly stable and reversible elastic recovery (>98%).

### 3.4 Electrical properties and strain response of the SFS nanocomposites

We studied the electrical conductivity and its responses to mechanical strain of the SFS nanocomposites. The findings are very interesting and show that the types of nanofillers and their morphologies and ratios, as well as the mechanical deformation rate, all have significant effects on the electrical properties. Three types of SFS nanocomposites were investigated and compared: SFS/CNT/Gr (90/5/5), SFS/CNT/CB (90/5/5), and SFS/CNT/CB (90/3/7). A comparative study of the first two types will show the effect of nanofiller dimension/morphology, and comparative study of the latter two types will show the effect of ratios between the nanofillers. The total weight fraction of the carbon nanofillers is fixed at 10% because at lower fractions the electrical conductivity is substantially lower. For instance, the electrical resistance of SFS/CNT/Gr (95/2.5/2.5) is about 500 times higher than that of SFS/CNT/Gr (90/5/5) (Fig. S6).

In the relaxed state with 0% strain, the SFS/CNT/Gr (90/5/5) nanocomposite shows a resistance of about 3.2 kΩ. With the increase of stretching strain, it shows a near linear increase in resistance (Fig. 4a); for instance, the resistance increases to 6.8 kΩ at 60% strain. Note that these resistance *vs.* strain data are obtained at the structural equilibrium state (after resistance reaches a stable value, usually about 3 minutes) at each strain. The corresponding *I*–*V* curves at different strains are also shown (Fig. 4a inset). In contrast, when 2D graphene is replaced with 0D carbon black, the SFS/CNT/CB (90/5/5) nanocomposite shows quite stable electrical resistance against strain (Fig. 4b). For instance, the resistance values at 0% and 60% strain are very close to each other at 6.6 kΩ and 6.5 kΩ, respectively. Moreover, when the ratio between CNTs and CB changes to 3 : 7, the SFS/CNT/CB (90/3/7) nanocomposite shows a substantial decrease in electrical resistance with increasing strain (Fig. 4c). For instance, its resistance decreases from 59 kΩ at 0% strain to 18 kΩ at 60% strain, which is different from that of both of the previous two types of nanocomposites. It is noted that the resistivity–strain relationship would follow the same trends due to the standardized sample dimensions.

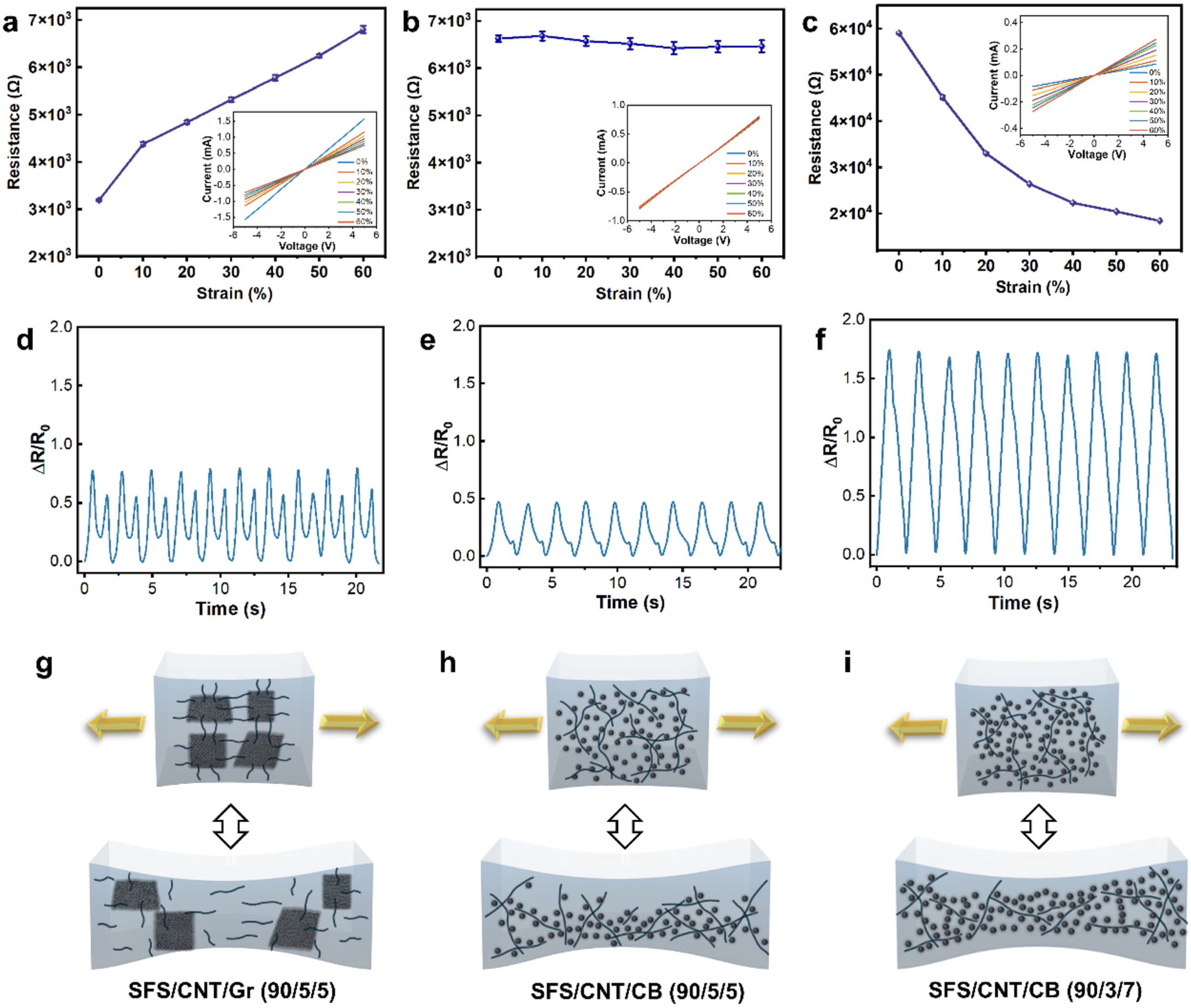

Fig. 4 (a–c) Resistance change as a function of tensile strain for (a) SFS/CNT/Gr (90/5/5), (b) SFS/CNT/CB (90/5/5), and (c) SFS/CNT/CB (90/3/7). Note that panel c has a different *Y* scale. The inset in each panel shows the corresponding *I*–*V* curves. (d–f) Relative resistance change ($\Delta R/R_0$) as a function of time during the cyclic deformation of (d) SFS/CNT/Gr (90/5/5), (e) SFS/CNT/CB (90/5/5), and (f) SFS/CNT/CB (90/3/7). Cyclic testing was conducted at a frequency of 0.45 Hz and a maximum strain of 50%. (g–i) Schematic of the proposed internal structural changes during mechanical deformation of the three types of SFS nanocomposites.

The dynamic responses of electrical resistance against mechanical strain are also quite different for the three types of SFS nanocomposites. The relative resistance change ($\Delta R/R_0$, absolute value) as a function of time during cyclic deformation of SFS/CNT/Gr (90/5/5) is shown in Fig. 4d. The resistance response in each stretching–relaxation cycle is not the typical monotonic increase until maximum strain and then decrease to the original value; instead, it shows a peak value during the stretching and another smaller peak value during the relaxation step. Such double-peak response of SFS/CNT/Gr (90/5/5) persists despite varying the maximum strain or cyclic loading frequencies (Fig. S7 and S8).

When graphene is replaced by carbon black, the SFS/CNT/CB (90/5/5) nanocomposite shows a different dynamic response (Fig. 4e), which still has two peaks during each stretching–relaxation cycle, but the peak during stretching is much more dominant. On the other hand, the SFS/CNT/CB (90/3/7) nanocomposite (Fig. 4f) shows a more typical dynamic response with an almost linear decrease in resistance until maximum strain followed by a linear increase during the relaxation step.

Such interesting and highly tunable electrical property responses can be explained by the differences in their internal structure, especially the conductive network formation and disruption during mechanical deformation. For the SFS/CNT/Gr (90/5/5) nanocomposite, the conductive pathways are formed by 1D CNT bridging the 2D graphene nanosheets (Fig. 4g). When the composite is under stretching, it is easy for such connections between CNTs and graphene to break, thus decreasing the number of conductive pathways and resulting in a resistance increase.

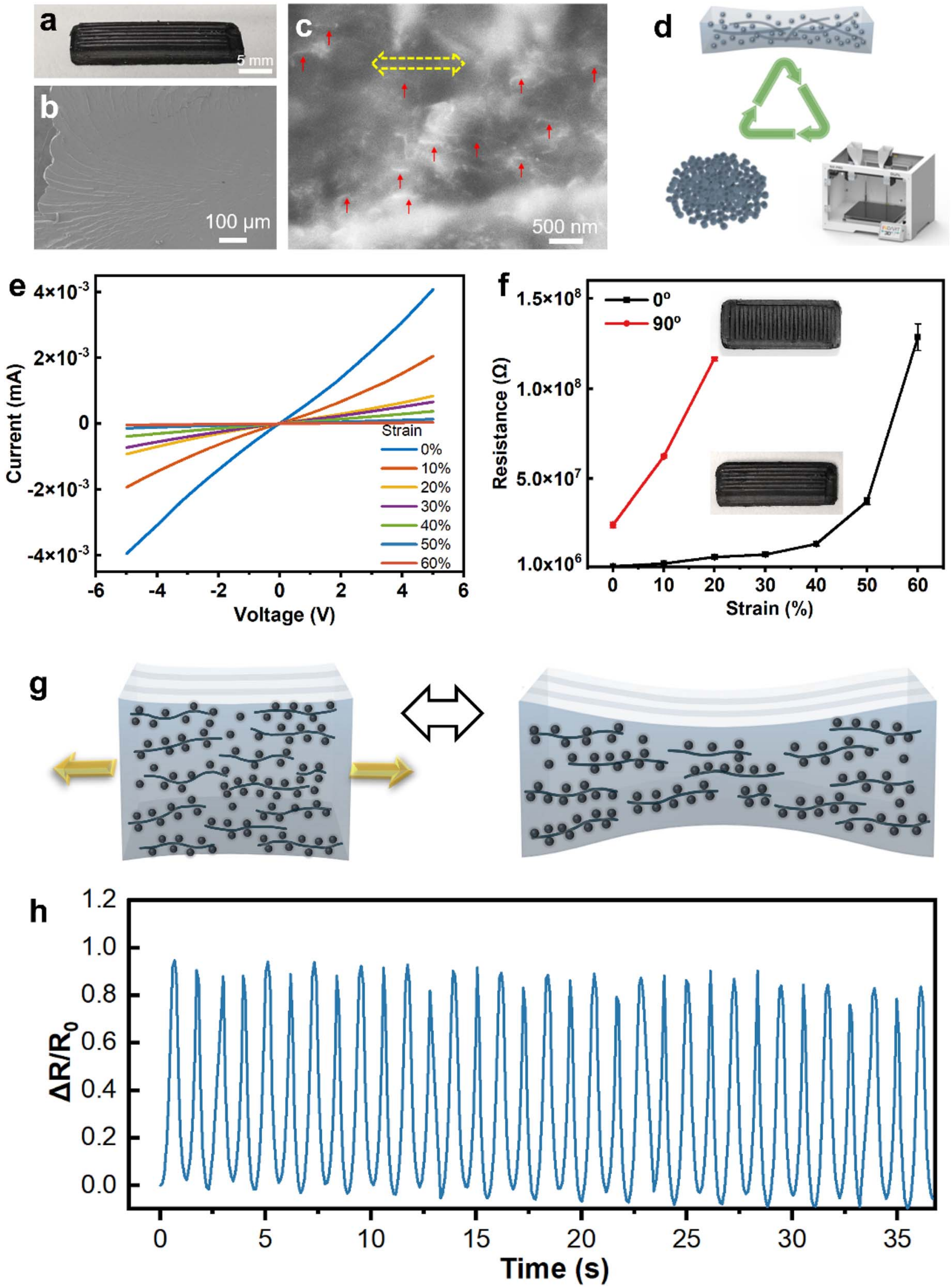

Fig. 5 (a) Photo of a pellet 3D-printed SFS/CNT/CB (90/3/7) nanocomposite with a rectangle shape. (b and c) Cross-section SEM images of the 3D-printed SFS/CNT/CB (90/3/7) nanocomposite at two different magnifications. Red arrows in (c) show representative locations where CNTs are aligned. (d) Schematic of recyclability of the SFS nanocomposites by pelletization and repeated 3D printing. (e) *I*–*V* curves of the 3D-printed SFS/CNT/CB (90/3/7) nanocomposite at different equilibrium strains. (f) Resistance changes as a function of equilibrium strains for the 3D-printed SFS/CNT/CB (90/3/7) nanocomposite. The black curve corresponds to the sample printed along the long axis (0°), and the red curve corresponds to the sample printed along the short axis (90°). (g) Schematic of the internal structural changes of 3D-printed SFS/CNT/CB during mechanical stretching. (h) Relative resistance change ($\Delta R/R_0$) of the 3D-printed SFS/CNT/CB (90/3/7) nanocomposite (printing direction of 0°) under cyclic stretching at 30% maximum strain at a frequency of 0.9 Hz.

For the SFS/CNT/CB (90/5/5) nanocomposite, the amount/density of 1D CNTs and 0D CB is similar; they also have a strong affinity to each other. Therefore, in the relaxed state, the conductive pathways are formed mostly by the interconnected network of curved CNTs with CB particles mostly located along the CNT network (Fig. 4h). Upon mechanical stretching (small to medium strain, before network disruption), the curved CNTs get straightened and better aligned along the stretching direction, and most of the junctions are maintained. That's why the conductivity is largely maintained despite the increase in strain.

On the other hand, for the SFS/CNT/CB (90/3/7) nanocomposite, CB is the majority nanofiller, so in the relaxed state, besides the conductive pathways formed by CNTs and CB, there are also excess CB nanoparticles dispersed in the SFS matrix without forming effective conductive channels (Fig. 4i). When mechanical stretching is applied, the excess CB nanoparticles can form additional conductive pathways due to the alignment and decreased interparticle distance. Therefore, the electrical resistance for the SFS/CNT/CB (90/3/7) nanocomposite decreases with increasing strain.

To explain the unusual double-peak responses of SFS/CNT/Gr nanocomposites when subjected to cyclic mechanical strains, we conducted additional experiments by fixing the amount of SFS and CNTs and varying the content of graphene in the three composites: SFS/CNT/Gr (90/5/2.5), SFS/CNT/Gr (90/5/5), and SFS/CNT/Gr (90/5/10). The resistance changes as a function of tensile strain and dynamic responses against cyclic strain are shown in Fig. S9 and S10. When the graphene content is low, namely SFS/CNT/Gr (90/5/2.5), the electrical response is very close to the conventional monotonic increase and then decreases to the original value. However, the two samples with higher graphene content show double-peak behavior.

This comparative study shows that the double-peak behavior is primarily due to the existence of 2D graphene, especially when it acts as the main conductive nanofiller. Due to its ultrathin structure and low bending stiffness, a fraction of graphene nanosheets are wrinkled or partially folded in the relaxed state (Fig. 3b). During the stretching cycle, with the increase in strain, these graphene nanosheets first flatten and increase the effective volume fraction of conductive nanofillers, which leads to a decrease in resistance. Then with further a increase in strain, the separation or distance between the conductive nanofillers increases, which leads to an increase in resistance. The reverse process occurs during the relaxation cycle.

### 3.5 Electrical properties and strain response of 3D-printed SFS nanocomposites

Pellet 3D printing was used as a novel method for fabricating soft and conductive SFS nanocomposites. We found that nanocomposites fabricated by pellet 3D printing show substantially different electrical properties and dynamic responses compared with those fabricated by solution casting. The internal structure of pellet 3D-printed SFS/CNT/CB (90/3/7) nanocomposites (Fig. 5a) is studied by cross-section SEM. The printed nanocomposites have a dense internal structure (Fig. 5b) without visible gaps or holes. A higher magnification SEM image shows fiber-like CNTs and CB NPs uniformly distributed in the polymer matrix. Moreover, the CNTs have a certain degree of preferential alignment along the printing direction marked by the yellow arrow (Fig. 5c).

Another advantage of our SFS nanocomposites is that they can be physically recycled and used for multiple cycles. Because there is no chemical crosslinking, our SFS nanocomposites can be reprocessed for new printing or recovery of polymers and nanofillers for new applications. For instance, the 3D-printed nanocomposite structures can be pelletized into composite pellets and then used as the starting raw material for new pellet 3D printing (Fig. 5d). This is demonstrated with the pellet-printed SFS/CNT/CB (90/3/7) nanocomposites (Fig. S11); the recycled and reprinted structures have comparable morphology and mechanical properties to the original ones.

The unique internal structure leads to very different electrical properties of the pellet 3D-printed SFS/CNT/CB (90/3/7) nanocomposite (Fig. 5e and f). The sample shows a significant increase in electrical resistance from $1.1 \times 10^6\ \Omega$ to $1.2 \times 10^8\ \Omega$ when the mechanical strain increases from 0% to 60%, in contrast to the decreasing trend of resistance for the solution-cast sample with the same composition. The probable reason for such a drastic difference is schematically shown in Fig. 5g. Due to the shear force in the extruder and printing nozzle during pellet 3D printing, there will be preferential orientation of stretched CNTs along the printing direction. A fraction of CB nanoparticles are located adjacent to CNTs, and the rest are dispersed in the SFS matrix. In the relaxed state, the junctions between the aligned CNTs are the primary pathways for electric conduction. Upon mechanical stretching, the stretched CNTs are easily separated from one another, and the density of conductive pathways is substantially reduced, which leads to an increase in electric resistance.

Moreover, the shear-induced alignment especially on the CNT component during pellet 3D printing also leads to anisotropic electrical properties. To demonstrate this, we printed SFS/CNT/CB (90/3/7) nanocomposites into the same rectangle shape but with different printing directions: parallel to the long axis (0°) and perpendicular to the long axis (90°) (Fig. 5f). The electrical conductivity along the long axis is much higher for the 0° sample than that of the 90° sample (resistance at the relaxed state: $1.1 \times 10^6\ \Omega$ *vs.* $2.5 \times 10^7\ \Omega$). These differences in electrical conductivity get more pronounced when the sample is stretched along the long axis. In addition, the dynamic response of 3D-printed SFS/CNT/CB (90/3/7) upon cyclic stretching is still fast and consistent over long cycles (Fig. 5h).

To summarize the major differences in properties of the 3D-printed and solution-cast SFS nanocomposites, we observed that the 3D-printed samples have comparable mechanical properties with the solution-cast ones, while the electrical responses are dramatically different due to the nanofiller dispersion and alignment. At the same composition, the 3D-printed nanocomposites show lower electrical conductivity but more pronounced changes in response to mechanical strain, which can be further tuned by controlling the printing direction.

### 3.6 Systematic study of SFS nanocomposite-based strain sensors

From the comparative study of multiple types of SFS nanocomposites and the fabrication approaches, it can be seen that the SFS/CNT/CB (90/3/7) nanocomposite from solution casting has the highest response sensitivity upon dynamic mechanical loading and therefore its strain sensor performance is more systematically studied, as discussed below. The electrical response of SFS/CNT/CB (90/3/7) against cyclic stretching with different maximum strains is shown in Fig. 6a. The relative resistance change is stable and consistent under all the different strain conditions. The peak value of $\Delta R/R_0$ also increases from 0.9 at 20% maximum strain to 2.8 at 80% maximum strain. The dynamic response of the SFS/CNT/CB (90/3/7) nanocomposite to applied strain (40% maximum) with varying frequencies from 0.125 to 0.4 Hz is shown in Fig. 6b (additional data are in Fig. S12). The responses are rapid and match with the mechanical deformation rate at all frequencies.

The long-term response stability of SFS nanocomposites against mechanical deformation (0.45 Hz, a maximum strain of 100%) is also studied (Fig. 6c). It can be seen that the sensitivity or magnitude of the electrical response of SFS/CNT/CB (90/3/7) nanocomposites has a gradual increase up to 3000 s. Then the response is highly stable and consistent across tens of thousands of cycles. The response rate of SFS/CNT/CB (90/3/7) nanocomposites is also tested with a fast deformation test as shown in Fig. 6d. It only takes 140 ms for the composite to respond and complete the significant resistance change.

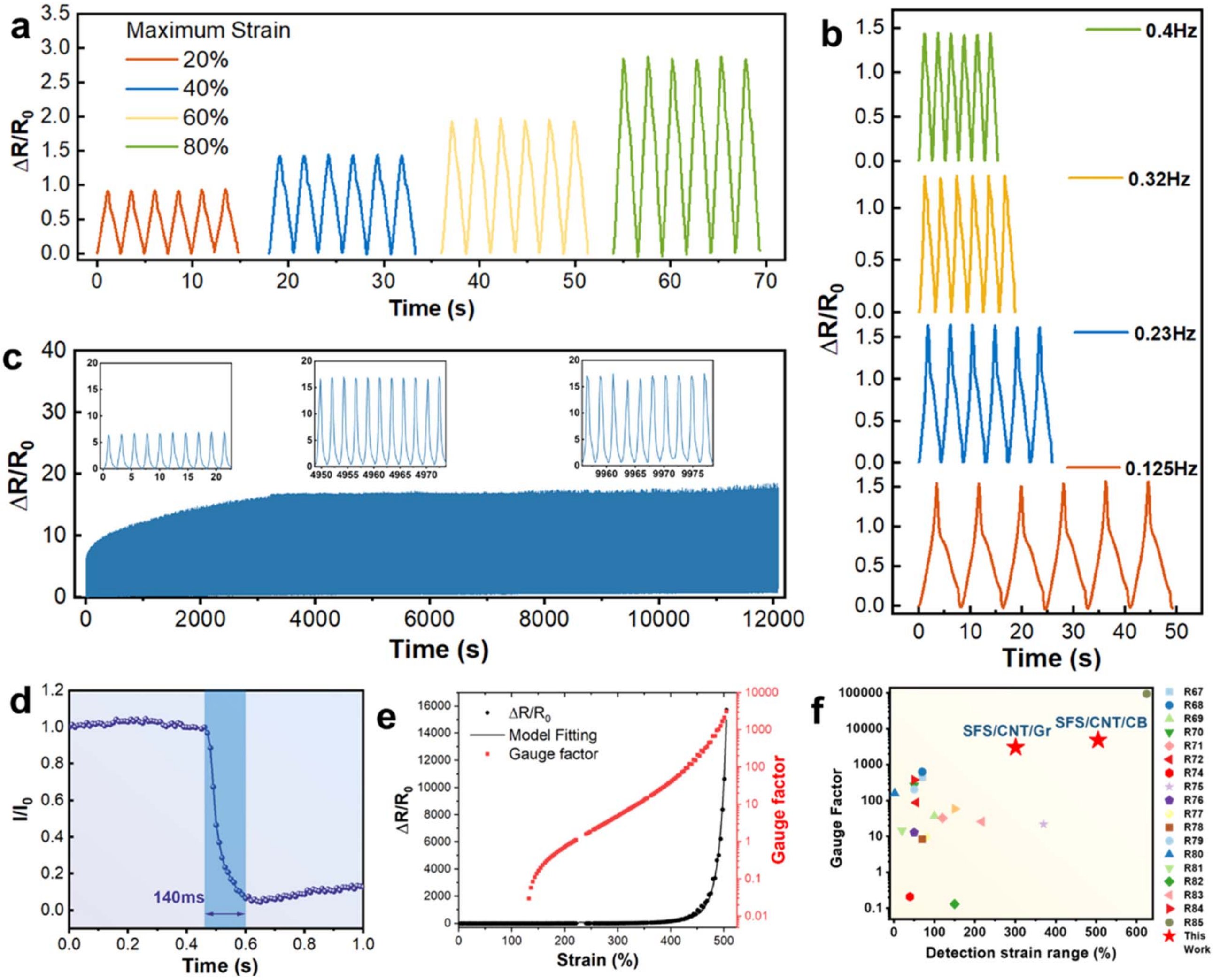

Fig. 6 (a) The relative resistance change ($\Delta R/R_0$) of SFS/CNT/CB (90/3/7) nanocomposites under cyclic stretching at different maximum strains at a frequency of 0.4 Hz. (b) The relative resistance change ($\Delta R/R_0$) of SFS/CNT/CB (90/3/7) under cyclic stretching at different frequencies with a maximum strain of 40%. (c) The cycling stability of SFS/CNT/CB (90/3/7) under 100% maximum strain with a duration of over 12 000 seconds. (d) Electrical response time of SFS/CNT/CB (90/3/7) during a rapid deformation. (e) The relative resistance change ($\Delta R/R_0$) and gauge factor as a function of strain for SFS/CNT/CB (90/3/7) with a maximum strain of 500%. The solid line is fitting of $\Delta R/R_0$ using the analytical model. (f) Comparison of the gauge factors of our SFS/CNT/CB and SFS/CNT/Gr composites with those of recently reported strain sensors.

The relative resistance change across a large strain range (up to 500%) is shown in Fig. 6e. It can be seen that when the strain reaches large values, there is an almost exponential increase in the resistance change with strain. For instance, the value of $\Delta R/R_0$ is about 15 at 300% strain, which rapidly increases to 200 at 400% strain and over 10 000 at 500% strain. We also used analytical modeling based on Simmons approximation theory to fit the relationship between relative resistance change and mechanical strain.[61] In our case,

$$\left(\frac{\Delta R}{R_0}\right) = \frac{R - R_0}{R_0} = (1 + E\varepsilon)\exp\left((A + FE)\varepsilon + B\varepsilon^2 + C\varepsilon^3 + D\varepsilon^4\right) - 1 \quad (1)$$

where $A$, $B$, $C$, and $D$ are material system dependent constants, and they represent the non-linear change in the number of conductive pathways at large strains. $E$ is another material system dependent constant that describes the change in the average spacing between neighboring conductive nanoparticles as a function of the applied strain. $F$ is a parameter that depends on the potential barrier between conductive nanoparticles. Detailed derivation and explanation of the model can be found in the SI. The model fitting matches very well with the experimental data.

Gauge factor $\left(\frac{\Delta R}{R_0}/\varepsilon\right)$ is frequently used to assess the performance of strain sensors and is also shown in Fig. 6e (red curve with the log scale). The SFS/CNT/CB (90/3/7) nanocomposite shows very large and fast-increasing gauge factors at strain above 200%. A similar trend of gauge factor is also obtained for SFS/CNT/Gr nanocomposites (Fig. S6). The performance of our SFS nanocomposites as strain sensors is compared with that in recent literature reports with similar material systems (Fig. 6f, see also Table S1).[67–85] It can be seen that our SFS nanocomposites show excellent performance in

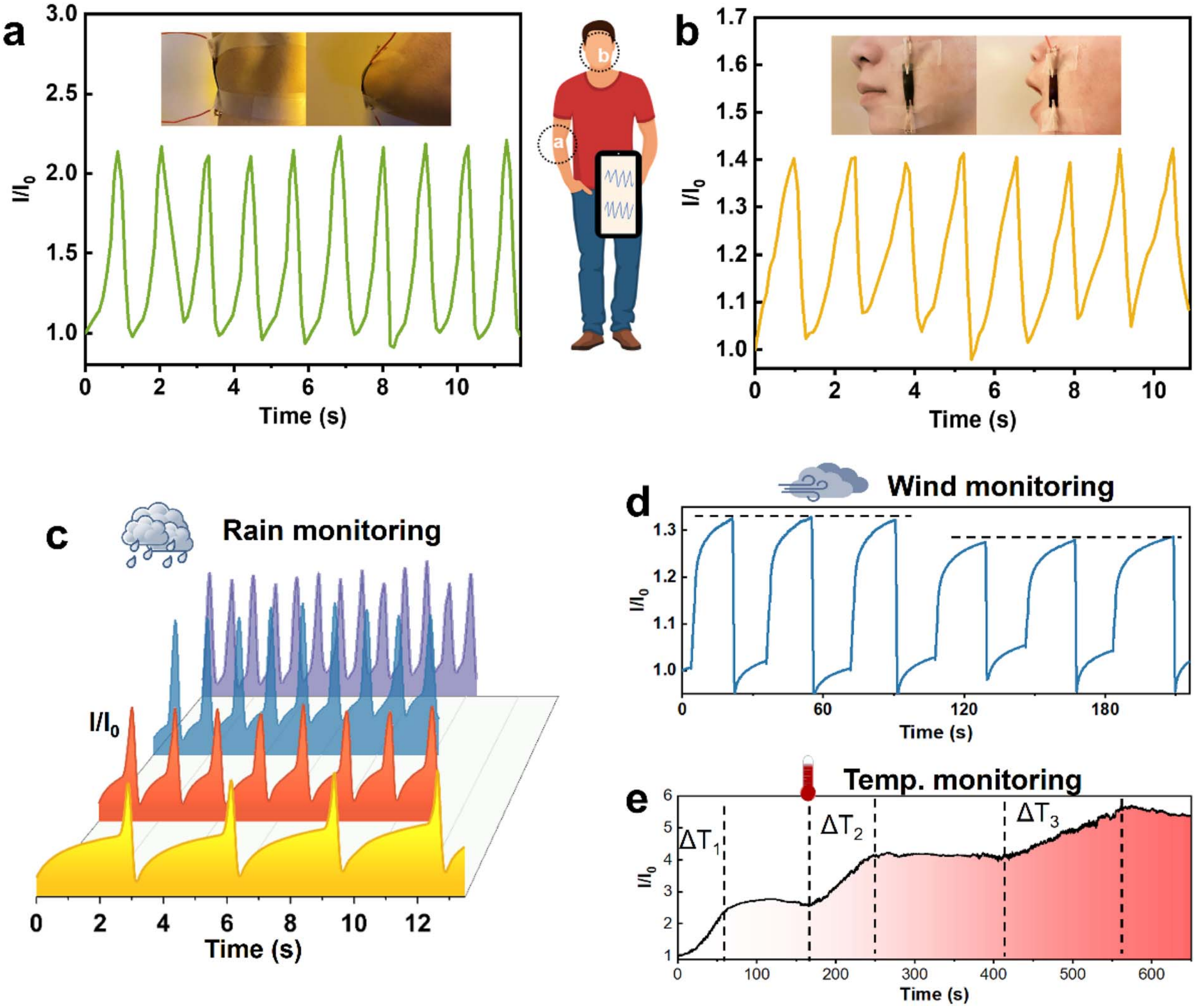

Fig. 7 Demonstration of the use of SFS/CNT/CB (90/3/7) nanocomposites in human motion monitoring and simulated weather monitoring. (a) Elbow flexion detection. (b) Mouth movement detection. (c) Monitoring of simulated raindrops with varying frequencies. (d) Monitoring of simulated wind blowing with two different speeds. (e) Monitoring of environmental temperature changes with three different heating and equilibrium stages.

terms of both the large detection range of strain and a high gauge factor at large strains.

### 3.7 Demonstration of wearable sensors and environment monitoring

The combination of high elasticity, low modulus, chemical stability, tunable conductivity, and rapid strain response of SFS nanocomposites enables their promising application in stretchable and wearable sensors. We demonstrate this by using SFS/CNT/CB (90/3/7) nanocomposites as sensors for human motion detection. The detection of repeated elbow flexion is shown in Fig. 7a. Mouth movement and closing are also accurately monitored (Fig. 7b), which can potentially be used for intelligent voice control. Subtle human motions such as rhythmic abdominal movement during breathing and finger bending detection are also demonstrated (Fig. S13), which is applicable to soft robotics.

Moreover, we also demonstrate that SFS/CNT/CB (90/3/7) nanocomposites can be used for accurate monitoring of environmental conditions including rain, wind, or temperature changes. For instance, we used water drops falling on the soft sensor to simulate rain detection, with the mass of each droplet being about 40 mg and a speed of 4.5 m s$^{-1}$ (from 1 meter height). Fig. 7c shows the electrical current response of such simulated rainfall with different frequencies. The nanocomposite can also be used to detect wind (Fig. 7d). The wind strokes that blow on the sample during the first 80 seconds have a speed of 17.0 m s$^{-1}$, and the subsequent wind strokes have a speed of 9.2 m s$^{-1}$. It can be seen that the magnitude of the current response is different at these two different wind speeds.

Last but not least, we demonstrate temperature monitoring using the SFS/CNT/CB (90/3/7) nanocomposite. Sensitive responses to multiple heating stages and temperatures can be obtained (Fig. 7e). For instance, in the first stage, the temperature increases from 20 °C to 44 °C and then remains stable for 100 s; in the second stage, the temperature further increases to 67 °C and remains stable for another 150 s; in the third stage, the temperature increases to 86 °C and then remains stable. The electrical current increases during each heating step and maintains stability when the temperature reaches equilibrium. The probable reason for the temperature-induced conductivity change is that the conductivity of CNTs increases with temperature due to the thermally activated process and increased charge carrier density.[86,87] As a result, our SFS/CNT/CB nanocomposites also show higher electrical conductivity at higher temperatures.

## 4. Conclusions

In summary, we developed a series of sustainable and 3D-printable soft nanocomposites by integrating an SFS TPE and carbon nanomaterials. Due to the excellent mechanical properties, chemical stability, and processability of SFS, these nanocomposites are flexible and stretchable (>1500%), with highly tunable internal structures and electrical properties, which are distinct from those of conventional soft composites with a petrochemical-based soft matrix and a single type of nanofiller. Pellet 3D printing is also used as a new and efficient approach for fabricating customizable 3D structures and devices based on SFS nanocomposites. The electrical responses of these SFS nanocomposites to mechanical deformation are highly tunable and diverse. Several key factors that determine these electrical responses including the type/geometry of carbon nanofillers, nanofiller loading, the ratio between the nanofillers, and the processing condition (3D printing *vs.* solution casting) were systematically investigated. Our SFS nanocomposites show superior performance as strain sensors in terms of the maximum strain range and gauge factor at large strains. We also demonstrate the application of these SFS nanocomposites in human motion detection and environment monitoring. The sustainable and 3D-printable SFS nanocomposites provide a material platform for future research in soft sensors, wearable electronics, and soft robotics.

## Author contributions

W. X. designed and supervised the research. X. L. conducted most of the experiments and data analysis. N. S., J. B., M. Y., and X. G. contributed to the experiments. X. L. and W. X. wrote the original manuscript. All authors reviewed and approved the final manuscript.

## Conflicts of interest

The authors declare no conflict of interest.

## Data availability

The data supporting this article have been included as part of the SI.

Additional characterization of the SFS copolymer and nanocomposites, including GPC, Raman, tensile testing, and mechanical and electrical property data. A detailed description of the analytical modeling of the resistance change as a function of mechanical strain. See DOI: https://doi.org/10.1039/d5ta04676a.

## Acknowledgements

W. X. gratefully acknowledges the startup support from the University of Akron. This work was also supported by the ACS PRF New Direction grant (No. 67730-ND7). We also would like to thank Kuraray Co. for providing the SEPTON polymer samples.

## References

1 T. Y. Kim, S. H. Hong, S. H. Jeong, H. Bae, S. Cheong, H. Choi and S. K. Hahn, *Adv. Mater.*, 2023, **35**, 2303401.
2 J. Gao, Y. Fan, Q. Zhang, L. Luo, X. Hu, Y. Li, J. Song, H. Jiang, X. Gao, L. Zheng, W. Zhao, Z. Wang, W. Ai, Y. Wei, Q. Lu, M. Xu, Y. Wang, W. Song, X. Wang and W. Huang, *Adv. Mater.*, 2022, **34**, 2107511.

3 C. Wang, D. Hwang, Z. Yu, K. Takei, J. Park, T. Chen, B. Ma and A. Javey, *Nat. Mater.*, 2013, **12**, 899–904.

4 L. Duan, D. R. D'hooge and L. Cardon, *Prog. Mater. Sci.*, 2020, **114**, 100617.

5 D. C. Kim, H. J. Shim, W. Lee, J. H. Koo and D. Kim, *Adv. Mater.*, 2020, **32**, 1902743.

6 K. Sim, Z. Rao, F. Ershad and C. Yu, *Adv. Mater.*, 2020, **32**, 1902417.

7 Y. He, D. Wu, M. Zhou, Y. Zheng, T. Wang, C. Lu, L. Zhang, H. Liu and C. Liu, *ACS Appl. Mater. Interfaces*, 2021, **13**, 15572–15583.

8 S. J. Paul, I. Elizabeth and B. K. Gupta, *ACS Appl. Mater. Interfaces*, 2021, **13**, 8871–8879.

9 Y. Jia, X. Yue, Y. Wang, C. Yan, G. Zheng, K. Dai, C. Liu and C. Shen, *Composites, Part B*, 2020, **183**, 107696.

10 M. Fan, L. Wu, Y. Hu, M. Qu, S. Yang, P. Tang, L. Pan, H. Wang and Y. Bin, *Adv. Compos. Hybrid Mater.*, 2021, **4**, 1039–1047.

11 S. C. B. Mannsfeld, B. C.-K. Tee, R. M. Stoltenberg, C. V. H.-H. Chen, S. Barman, B. V. O. Muir, A. N. Sokolov, C. Reese and Z. Bao, *Nat. Mater.*, 2010, **9**, 859–864.

12 W. Yang, J.-J. Liu, L.-L. Wang, W. Wang, A. C. Y. Yuen, S. Peng, B. Yu, H.-D. Lu, G. H. Yeoh and C.-H. Wang, *Composites, Part B*, 2020, **188**, 107875.

13 G. Georgousis, K. Roumpos, E. Kontou, A. Kyritsis, P. Pissis, S. Koutsoumpis, M. Mičušík and M. Omastová, *Composites, Part B*, 2017, **131**, 50–61.

14 Y.-R. Ding, C.-H. Xue, X.-J. Guo, X. Wang, S.-T. Jia and Q.-F. An, *Chem. Eng. J.*, 2021, **409**, 128199.

15 H. Zhang, N. He, B. Wang, B. Ding, B. Jiang, D. Tang and L. Li, *Adv. Mater.*, 2023, **35**, 2300398.

16 J. Chen, L. Zhang, Y. Tu, Q. Zhang, F. Peng, W. Zeng, M. Zhang and X. Tao, *Nano Energy*, 2021, **88**, 106272.

17 D. Xiang, X. Zhang, E. Harkin-Jones, W. Zhu, Z. Zhou, Y. Shen, Y. Li, C. Zhao and P. Wang, *Composites, Part A*, 2020, **129**, 105730.

18 Q. Zou, K. He, J. Ou-Yang, Y. Zhang, Y. Shen and C. Jin, *ACS Appl. Mater. Interfaces*, 2021, **13**, 14479–14488.

19 S. Liu, Y. Wu, L. Jiang, W. Xie, B. Davis, M. Wang, L. Zhang, Y. Liu, S. Xing, M. D. Dickey and W. Bai, *ACS Appl. Mater. Interfaces*, 2024, **16**, 46538–46547.

20 S. Mousavi, D. Howard, F. Zhang, J. Leng and C. H. Wang, *ACS Appl. Mater. Interfaces*, 2020, **12**, 15631–15643.

21 T. Xiao, C. Qian, R. Yin, K. Wang, Y. Gao and F. Xuan, *Adv. Mater. Technol.*, 2021, **6**, 2000745.

22 Y. He, M. Zhou, M. H. H. Mahmoud, X. Lu, G. He, L. Zhang, M. Huang, A. Y. Elnaggar, Q. Lei, H. Liu, C. Liu and I. H. E. Azab, *Adv. Compos. Hybrid Mater.*, 2022, **5**, 1939–1950.

23 X. Zhang, L. Ke, X. Zhang, F. Xu, Y. Hu, H. Lin and J. Zhu, *ACS Appl. Mater. Interfaces*, 2022, **14**, 25753–25762.

24 L. Zhou, J. Fu, Q. Gao, P. Zhao and Y. He, *Adv. Funct. Mater.*, 2020, **30**, 1906683.

25 S. Tang, J. Li, R. Wang, J. Zhang, Y. Lu, G. Hu, Z. Wang and L. Zhang, *SusMat*, 2022, **2**, 2–33.

26 D. Jung, C. Lim, C. Park, Y. Kim, M. Kim, S. Lee, H. Lee, J. H. Kim, T. Hyeon and D. Kim, *Adv. Mater.*, 2022, **34**, 2200980.

27 R. Bonart, *Polymer*, 1979, **20**, 1389–1403.

28 R. J. Spontak and N. P. Patel, *Curr. Opin. Colloid Interface Sci.*, 2000, **5**, 333–340.

29 M. Steube, T. Johann, R. D. Barent, A. H. E. Müller and H. Frey, *Prog. Polym. Sci.*, 2022, **124**, 101488.

30 P. Sahu, J. Young Ko, J. Uk Ha and J. S. Oh, *Ind. Eng. Chem. Res.*, 2023, **62**, 8726–8735.

31 C. Wahlen and H. Frey, *Macromolecules*, 2021, **54**, 7323–7336.

32 P. B. V. Scholten, C. Detrembleur and M. A. R. Meier, *ACS Sustainable Chem. Eng.*, 2019, **7**, 2751–2762.

33 K. R. Benjamin, I. R. Silva, J. P. Cherubim, D. McPhee and C. J. Paddon, *J. Braz. Chem. Soc.*, 2016, **27**, 1339–1345.

34 S. Hiromitsu, Y. Uehara, and M. Kato, *US Pat.*, US20160108228A1, 2016.

35 D. J. McPhee, *US Pat.*, US7759444B1, 2010.

36 D. H. Lamparelli, V. Paradiso, F. D. Monica, A. Proto, S. Guerra, L. Giannini and C. Capacchione, *Macromolecules*, 2020, **53**, 1665–1673.

37 P. Sahu and J. S. Oh, *Ind. Eng. Chem. Res.*, 2022, **61**, 11815–11824.

38 P. Martins, N. Pereira, A. C. Lima, A. Garcia, C. Mendes-Filipe, R. Policia, V. Correia and S. Lanceros-Mendez, *Adv. Funct. Mater.*, 2023, **33**, 2213744.

39 N. Shen, J. Bu, M. E. Prévôt, T. Hegmann, J. P. Kennedy and W. Xu, *Macromol. Rapid Commun.*, 2023, **44**, 2200109.

40 M. Yang, J. Bu, N. Shen, S. Liu and W. Xu, *Adv. Mater. Technol.*, 2025, **10**, 2400890.

41 S. Liu, M. Yang, C. Smarr, G. Zhang, H. Barton and W. Xu, *ACS Appl. Bio Mater.*, 2024, **7**, 3247–3257.

42 B. Duncan, D. Beck, P. Miller, R. Benz, K. Ledford, A. Rosh-Gorsky and M. Smith, *ACS Mater. Lett.*, 2024, **6**, 720–728.

43 Z. Jiang, O. Erol, D. Chatterjee, W. Xu, N. Hibino, L. H. Romer, S. H. Kang and D. H. Gracias, *ACS Appl. Mater. Interfaces*, 2019, **11**, 28289–28295.

44 N. Shen, L. Duan, M. Yang, S. Liu and W. Xu, *MRS Commun.*, 2022, **12**, 597–602.

45 S. Park, W. Shou, L. Makatura, W. Matusik and K. (Kelvin) Fu, *Matter*, 2022, **5**, 43–76.

46 D. G. Bekas, Y. Hou, Y. Liu and A. Panesar, *Composites, Part B*, 2019, **179**, 107540.

47 W. Xu, S. Jambhulkar, Y. Zhu, D. Ravichandran, M. Kakarla, B. Vernon, D. G. Lott, J. L. Cornella, O. Shefi, G. Miquelard-Garnier, Y. Yang and K. Song, *Composites, Part B*, 2021, **223**, 109102.

48 M. Zhou, J. Li, P. Reyes, M. Erkoç, G. Wang, M. Edeleva, N. Zhu, M. Deng, L. Cardon and D. R. D'hooge, *Nano Energy*, 2025, **135**, 110629.

49 A. Osman and J. Lu, *Mater. Sci. Eng., R*, 2023, **154**, 100734.

50 N. Shen, S. Liu, P. Kasbe, F. Khabaz, J. P. Kennedy and W. Xu, *ACS Appl. Polym. Mater.*, 2021, **3**, 4554–4562.

51 J. Bu, N. Shen, Z. Qin and W. Xu, *Cell Rep. Phys. Sci.*, 2023, **4**, 101604.

52 B. Duncan, R. D. Weeks, B. Barclay, D. Beck, P. Bluem, R. Rojas, M. Plaut, J. Russo, S. G. M. Uzel, J. A. Lewis and T. Fedynyshyn, *Adv. Mater. Technol.*, 2023, **8**, 2201496.

53 N. Zhou, Y. Bekenstein, C. N. Eisler, D. Zhang, A. M. Schwartzberg, P. Yang, A. P. Alivisatos and J. A. Lewis, *Sci. Adv.*, 2019, **5**, eaav8141.

54 M. Kim, S. Nian, D. A. Rau, B. Huang, J. Zhu, G. Freychet, M. Zhernenkov and L.-H. Cai, *Cell Rep. Phys. Sci.*, 2024, **4**, 98–108.

55 B. B. Patel, D. J. Walsh, D. H. Kim, J. Kwok, B. Lee, D. Guironnet and Y. Diao, *Sci. Adv.*, 2020, **6**, eaaz7202.

56 F. Pignatelli and G. Percoco, *Prog. Addit. Manuf.*, 2022, **7**, 1363–1377.

57 A. La Gala, R. Fiorio, M. Erkoç, L. Cardon and D. R. D'hooge, *Processes*, 2020, **8**, 1522.

58 D. V. A. Ceretti, M. Edeleva, L. Cardon and D. R. D'hooge, *Molecules*, 2023, **28**, 2344.

59 M. Zhou, P. J. González, L. Van Haasterecht, A. Soylu, M. Mihailovski, P. Van Zuijlen and M. L. Groot, *Biomech. Model. Mechanobiol.*, 2024, **23**, 911–925.

60 N. S. Karode, A. Poudel, L. Fitzhenry, S. Matthews, P. R. Walsh and A. B. Coffey, *Polym. Test.*, 2017, **62**, 268–277.

61 D. Xiang, X. Zhang, Y. Li, E. Harkin-Jones, Y. Zheng, L. Wang, C. Zhao and P. Wang, *Composites, Part B*, 2019, **176**, 107250.

62 S. Yu, X. Wang, H. Xiang, L. Zhu, M. Tebyetekerwa and M. Zhu, *Carbon*, 2018, **140**, 1–9.

63 P. Xu, S. Wang, A. Lin, H.-K. Min, Z. Zhou, W. Dou, Y. Sun, X. Huang, H. Tran and X. Liu, *Nat. Commun.*, 2023, **14**, 623.

64 J. M. Clough, C. Creton, S. L. Craig and R. P. Sijbesma, *Adv. Funct. Mater.*, 2016, **26**, 9063–9074.

65 T. Schmaltz, L. Wormer, U. Schmoch and H. Döscher, *2D Mater.*, 2024, **11**, 022002.

66 F. Orozco, A. Salvatore, A. Sakulmankongsuk, D. R. Gomes, Y. Pei, E. Araya-Hermosilla, A. Pucci, I. Moreno-Villoslada, F. Picchioni and R. K. Bose, *Polymer*, 2022, **260**, 125365.

67 Y. Hu, T. Huang, H. Lin, L. Ke, W. Cao, C. Chen, W. Wang, K. Rui and J. Zhu, *J. Mater. Chem. A*, 2022, **10**, 928–938.

68 Q. Duan, B. Lan and Y. Lv, *ACS Appl. Mater. Interfaces*, 2022, **14**, 1973–1982.

69 S. Zhu, H. Sun, Y. Lu, S. Wang, Y. Yue, X. Xu, C. Mei, H. Xiao, Q. Fu and J. Han, *ACS Appl. Mater. Interfaces*, 2021, **13**, 59142–59153.

70 X.-C. Tan, J.-D. Xu, J.-M. Jian, G.-H. Dun, T.-R. Cui, Y. Yang and T.-L. Ren, *ACS Nano*, 2021, **15**, 20590–20599.

71 S. Wu, S. Peng, Z. J. Han, H. Zhu and C. H. Wang, *ACS Appl. Mater. Interfaces*, 2018, **10**, 36312–36322.

72 G. Li, K. Dai, M. Ren, Y. Wang, G. Zheng, C. Liu and C. Shen, *J. Mater. Chem. C*, 2018, **6**, 6575–6583.

73 Y. Jiang, Y. Chen, W. Wang and D. Yu, *Colloids Surf., A*, 2021, **629**, 127477.

74 A. Shaker, A. H. Hassanin, N. M. Shaalan, M. A. Hassan and A. A. El-Moneim, *Smart Mater. Struct.*, 2019, **28**, 075029.

75 Y. Wang, W. Li, Y. Zhou, L. Jiang, J. Ma, S. Chen, S. Jerrams and F. Zhou, *J. Mater. Sci.*, 2020, **55**, 12592–12606.

76 L. Lu, X. Wei, Y. Zhang, G. Zheng, K. Dai, C. Liu and C. Shen, *J. Mater. Chem. C*, 2017, **5**, 7035–7042.

77 Z. Jia, Z. Li, S. Ma, W. Zhang, Y. Chen, Y. Luo, D. Jia, B. Zhong, J. M. Razal, X. Wang and L. Kong, *J. Colloid Interface Sci.*, 2021, **584**, 1–10.

78 Q. Xia, S. Wang, W. Zhai, C. Shao, L. Xu, D. Yan, N. Yang, K. Dai, C. Liu and C. Shen, *Compos. Commun.*, 2021, **26**, 100809.

79 Y. Wang, F. Wang, S. Yazigi, D. Zhang, X. Gui, Y. Qi, J. Zhong and L. Sun, *Carbon*, 2021, **173**, 849–856.

80 Z. Liu, D. Qi, P. Guo, Y. Liu, B. Zhu, H. Yang, Y. Liu, B. Li, C. Zhang, J. Yu, B. Liedberg and X. Chen, *Adv. Mater.*, 2015, **27**, 6230–6237.

81 N. Qaiser, F. Al-Modaf, S. M. Khan, S. F. Shaikh, N. El-Atab and M. M. Hussain, *Adv. Funct. Mater.*, 2021, **31**, 2103375.

82 F. Zhang, D. Ren, L. Huang, Y. Zhang, Y. Sun, D. Liu, Q. Zhang, W. Feng and Q. Zheng, *Adv. Funct. Mater.*, 2021, **31**, 2107082.

83 M. Lin, Z. Zheng, L. Yang, M. Luo, L. Fu, B. Lin and C. Xu, *Adv. Mater.*, 2022, **34**, 2107309.

84 F. Zhang, L. Guo, Y. Shi, Z. Jin, Y. Cheng, Z. Zhang, C. Li, Y. Zhang, C. H. Wang, W. Feng and Q. Zheng, *Chem. Eng. J.*, 2023, **452**, 139664.

85 L. Duan, M. Spoerk, T. Wieme, P. Cornillie, H. Xia, J. Zhang, L. Cardon and D. R. D'hooge, *Compos. Sci. Technol.*, 2019, **171**, 78–85.

86 S. Fujita and A. Suzuki, *J. Appl. Phys.*, 2010, **107**, 013711.

87 M. Mohiuddin and S. V. Hoa, *Compos. Sci. Technol.*, 2011, **72**, 21–27.